Frequency distribution of dissipation of energy of ocean waves by sea ice using data from Wave Array 3 of the ONR "Sea State" field experiment

W. Erick Rogers

Naval Research Laboratory, Stennis Space Center, MS, USA

Michael H. Meylan

School of Mathematical and Physical Science, University of Newcastle, Newcastle, New South Wales, Australia

Alison L. Kohout

National Institute of Water and Atmospheric Research, Christchurch, New Zealand

Corresponding author: W. Erick Rogers (erick.rogers@nrlssc.navy.mil)

Listing of tables and figures

Executive Summary

This report is an addendum to the earlier report, Rogers et al. (2018). The model-data inversion (to create distributions of dissipation rate as a function of frequency) of that report is repeated using ice concentration from the AMSR2 instrument processed using the *Bootstrap* algorithm. The resulting distributions (or profiles) are averaged, using groupings by buoy type, ice type, and ice concentration. The average profiles are fitted to polynomials following Meylan et al. (2014) and compared to other data and average profiles from the literature. Unlike the Rogers et al. (2018) study, we focus specifically on one particular wave experiment, Wave Array #3 of the Sea State cruise.

1. Introduction

Declining ice cover in the Arctic has motivated research to study the implications for interactions between the atmosphere, ocean circulation, sea ice, and ocean waves. The U.S. Office of Naval Research funded a field study during the autumn ice advance (late September to early November) in the Beaufort Sea and nearby waters, with this purpose in mind. Through a better understanding of these interactions, it is possible to produce more reliable forecasts of the ocean environment, which is valuable for military and commercial activities at high latitudes. This field study, the "Sea State cruise", is described in Thomson (2015), Wadhams and Thomson (2015), Rogers et al. (2018) (denoted "R18" here), and Thomson et al. (2018). The R18 report and the present report deal with prediction of ocean waves, and more specifically the dissipation of wave energy caused by sea ice.

Model introduction

The model used is WAVEWATCH III®, henceforth denoted "WW3", see Tolman (1991) and WW3DG (2016). In early versions of this model, e.g. Tolman (2009), regions of high ice concentration are treated as land, regions of low ice concentration are treated as open water, and in intermediate concentrations, the removal of wave energy by sea ice was uniform in frequency space. The increased interest in high latitudes, the expansion of open water in the Arctic which allows for greater fetch for wave generation (Thomson and Rogers 2012), and the enhanced penetration of wave energy into higher and higher latitudes (e.g. Thomson et al. 2016) motivates improvements on this old, simplistic approach. In more recent versions, e.g. Tolman et al. (2014) and WW3DG (2016), the ocean is not treated as land, even for 100% ice concentration, and wave energy is non-zero everywhere in the Arctic Ocean[1]. Perhaps more importantly, dissipation rate is dependent on wave frequency, $k_i(f)$, with most methods applying stronger dissipation to shorter waves (i.e., the intuitive behavior). A review of these methods can be found in R18.

Data collected during the Sea State cruise was used by Collins and Rogers (2017) and R18 to develop a parametric form of $k_i(f)$ and this is already being applied routinely in WW3 implementations at NRL: for regional and global models; for hindcast and realtime models. However much work still remains to be done. A single parametric model for $k_i(f)$ is an improvement over the older approach, but is not expected to be accurate for all ice conditions. If we are to continue using parametric models of $k_i(f)$, accuracy can be improved by selecting a parametric model based on knowledge of ice concentration, thickness, and type. (In an

[1] This is with the exception of the North Pole, which is masked to prevent a singularity that is caused by the model's angle convention (Rogers and Campbell 2009).

operational context, estimates of the first two are available, but not yet the third.). The decay rate almost certainly also depends on the wave amplitude, i.e. there are nonlinear dependencies on decay. Field campaigns such as the Sea State cruise are crucial for mapping these dependencies.

Observations introduction

In Section 2, model-data inversion is used to estimate these *dissipation profiles*. The method is described in Rogers et al. (2016) and R18. Observational data for this inversion is taken from three types of drifting wave buoys. While there is a complete description in R18, we list here the groups that provided the data:

- SWIFT buoys, provided by J. Thomson, Madison Smith, and others at the Applied Physics Laboratory (University of Washington). See Thomson (2012).
- UK buoys, provided by M. Doble (Polar Scientific) and P. Wadhams (U. Cambridge)
- NIWA buoy, provided by co-author A. Kohout (New Zealand National Institute of Water and Atmospheric Research). See Kohout et al. (2015).

In R18, wave model performance is evaluated for seven different wave buoy deployments. In the present study, we focus on only the largest of the seven deployments. This is Wave Array #3 (WA3), which was also the focus of Rogers et al. (2016)[2]. WA3 was the *flagship* wave experiment of the cruise, spanning several days (October 10 0700 UTC to October 14 2330 UTC), with measured significant waveheight over 4.5 m. Descriptions can be found in Thomson (2015), Wadhams and Thomson (2015), and R18. Example positions of the three buoy types during WA3 are shown in Figure 1.

Shorthand for references

We use a shorthand notation for some references as follows:

- M14 is Meylan et al. (2014)
- R16 is Rogers et al. (2016)
- C17 is Collins and Rogers (2017)
- R18 is Rogers et al. (2018)
- M18 is Meylan et al. (2018)

2. Inversion profiles for WA3 using Bootstrap AMSR2

A full description of the inversion process is described in R16 and R18. To summarize, a dissipation rate $k_i(f)$ is found which provides a match between the model spectrum and the buoy spectrum. Thus, it is a model-data inversion, and we obtain an inversion profile $k_i(f)$ for each model spectrum. This inversion is performed for eight frequency bins, coarsened from the native resolution of the model and the buoy spectra provided.

The inversion results of R16 were used to create a $k_i(f)$ step function for use in WW3. The method is summarized in Section 7 here. That step function is denoted as "IC4M6H" in C17 and R18. In the present report, we refer to it as "IC4M6H1". The inversion results of R18 were also used to create a $k_i(f)$ step function for use in WW3, again summarized in Section 7 here. That is referred to as "IC4M6H2" in R18 and herein. Four new step functions, "IC4M6H3", "WA3-SWIFT", "WA3-UK", and "WA3-NIWA" are introduced in this report. All four new step

[2] And others, more recently, in papers to be published in the Sea State "Special Issue" for JGR Oceans.

functions are created from the same inversion, using different averaging procedures as summarized in Section 7.

The inversion of this report is similar to that described in R18, but the following changes have been made to the WW3 simulations:

- Wind forcing is from NAVGEM (Hogan et al. 2014), with resolution near 0.28°. In R18, the forcing for the model used in the inversions was at 0.5° resolution.
- Air-sea temperature differences are used to modify drag: this corresponds to the "STAB3" switch in WW3. This change is not expected to be important here and is only mentioned for the sake of completeness. WW3 predicts that thermal stability does not have a significant impact on the wave growth during WA3 since air-sea temperature differences were small. This effect was studied in a sensitivity analysis in R18, but there are some differences between the application here and in the earlier sensitivity analysis: In R18, the forcing from 0.28° resolution NAVGEM including air-sea temperature differences was only employed for the inner WW3 grid. Here, we apply this enhanced forcing to both WW3 grids. Also, in R18, GOFS 3.1 was used for SST, whereas here, we use SST that comes with the NAVGEM analyses.
- Ice concentration is from AMSR2 swath data with high temporal resolution, as used in the inversion of R18 which was used to create the "IC4M6H2" of that report. However, where R18 use the NASA Team 2 (NT2) algorithm (Markus and Cavalieri 2000, 2009) to process the AMSR2 data, the Bootstrap algorithm (Comiso et al. 2003) is used here. Like R18, AMSR2 swath processing was performed by Dr. Li (NRL-DC). Fields from both algorithms were compared against SAR data in Section 4 of R18, but Bootstrap fields were not applied in WW3 in R18. Looking at two time periods (9 September and 11 October 2015), R18 found that the Bootstrap fields tend to show ice over a larger area, while the NT2 fields tend to show larger variability (lower minima and larger maxima) in regions of partial ice cover. An example, during WA3, is shown in Figure 1.

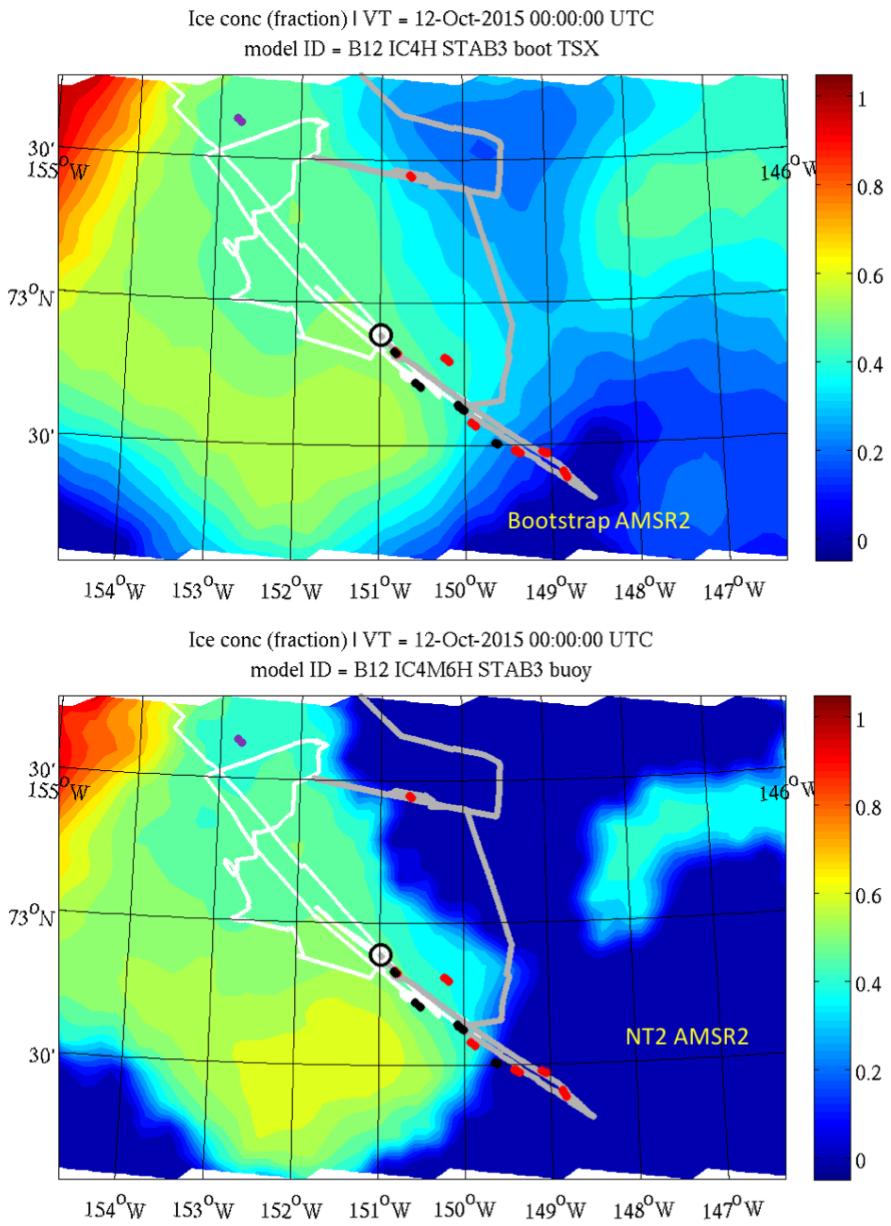

Figure 1. Comparison of AMSR2 ice concentration fields at an example time period during WA3: 2015 October 12 0000 UTC. Top panel: Bootstrap algorithm. Lower panel: NASA Team 2 algorithm. Concentration is indicated using color scaling, as a fraction, so values are 0.0 to 1.0. The white line indicates future ship track. Gray line indicates past ship track. Black circle indicates present ship position. Red dots indicate SWIFT buoys (±1 hour). Black dots indicate UK buoys (±1 hour). Purple dots indicate NIWA buoy (±1 hour).

Figure 2 to Figure 4 show results from the new inversion. Individual inversion profiles (thin lines) are color-scaled by AMSR2 ice concentration. The IC4M6H1 profile (thick black line, from R16 and C17) and IC4M6H2 profile (thick purple line, from R18) are shown as a reference.

Some subjective thresholds affect the number of profiles. The number of profiles in turn, affects plotting (e.g. how many profiles to show on a plot) and averaging (i.e. distillation of many profiles from a particular wave experiment and particular buoy type into a single representative profile). The thresholds are as follows:

1) option to exclude non-monotonic profiles
2) option to exclude cases with low ice concentration, since the inversion tends to be less successful in those cases (see discussion in Section 3)
3) option to exclude cases where the inversion succeeded only for a few (e.g. 2 or 3) of the eight frequency bins. Below, we refer to a bin for which the inversion procedure found a solution as a "good bin". Examples of failed inversions are given in R18.

For example, with WA3, we performed the inversion on 609 SWIFT buoy spectra. For the inversion herein (using Bootstrap AMSR2), the number reduces as follows:

- 542 cases with at least 4 good bins
- 388 cases with ice concentration a_{ice} over 0.3
- 372 cases with a_{ice} > 0.3 and at least 4 good bins
- 231 cases with a_{ice} > 0.3 and monotonicity
- 218 cases with a_{ice} > 0.3 and at least 4 good bins and monotonicity

For the inversion of R18, using NT2 AMSR2, we have:

- 324 cases with at least 4 good bins
- 188 cases with ice concentration a_{ice} over 0.3
- 188 cases with a_{ice} > 0.3 and at least 4 good bins
- 119 cases with a_{ice} > 0.3 and monotonicity
- 119 cases with a_{ice} > 0.3 and at least 4 good bins and monotonicity

Since both the ice concentration criterion and "good bin" criterion relate to the success of the inversion, they are semi-redundant. In the NT2 case, once the a_{ice} criterion is applied, the "good bin" criterion is unnecessary.

The Bootstrap and NT2 cases have a different success rate because of the strong dependence of inversion success on ice concentration. The inversion provides a null solution (failure) in cases where the model outcome (energy density at buoy location) is insufficiently sensitive to the S_{ice} source function. This happens most often in cases where the local ice concentration is low. As shown in R18, the Bootstrap fields tend to have larger regions of non-zero ice concentration, whereas the NT2 fields have higher maximum ice concentrations.

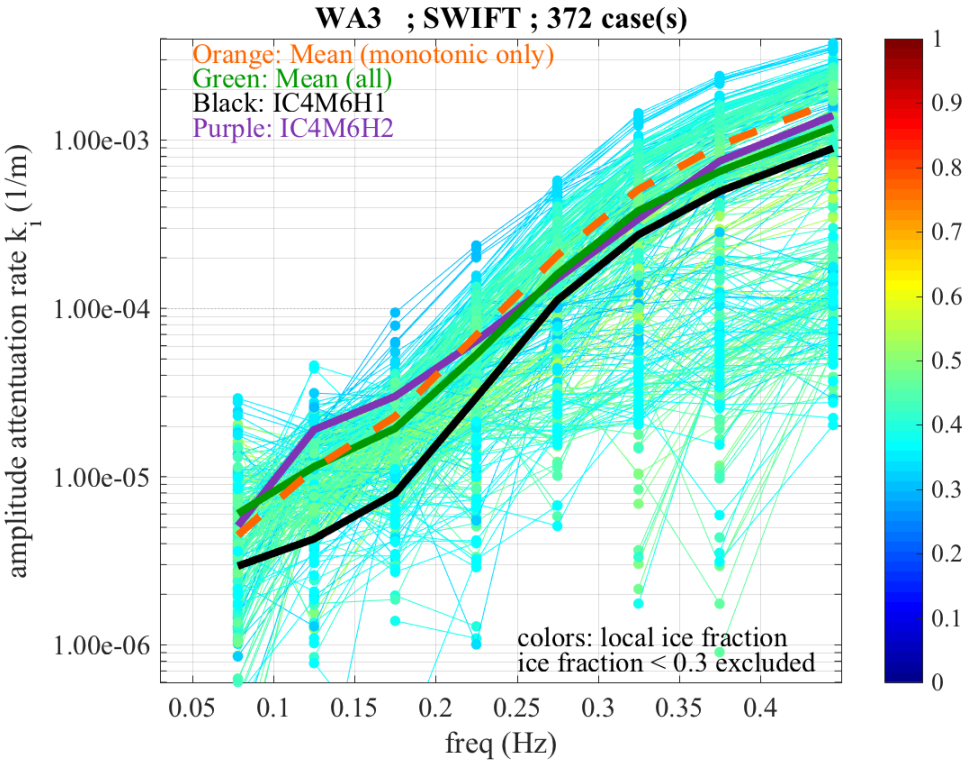

Figure 2. Inversion results for WA3, SWIFT buoys. Color scaling is by ice concentration. The thick green line is an average of the inversion profiles shown here, and the thick orange line is an average excluding non-monotonic profiles. The IC4M6H1 profile (thick black line) and IC4M6H2 profile (thick purple line) are shown as a reference.

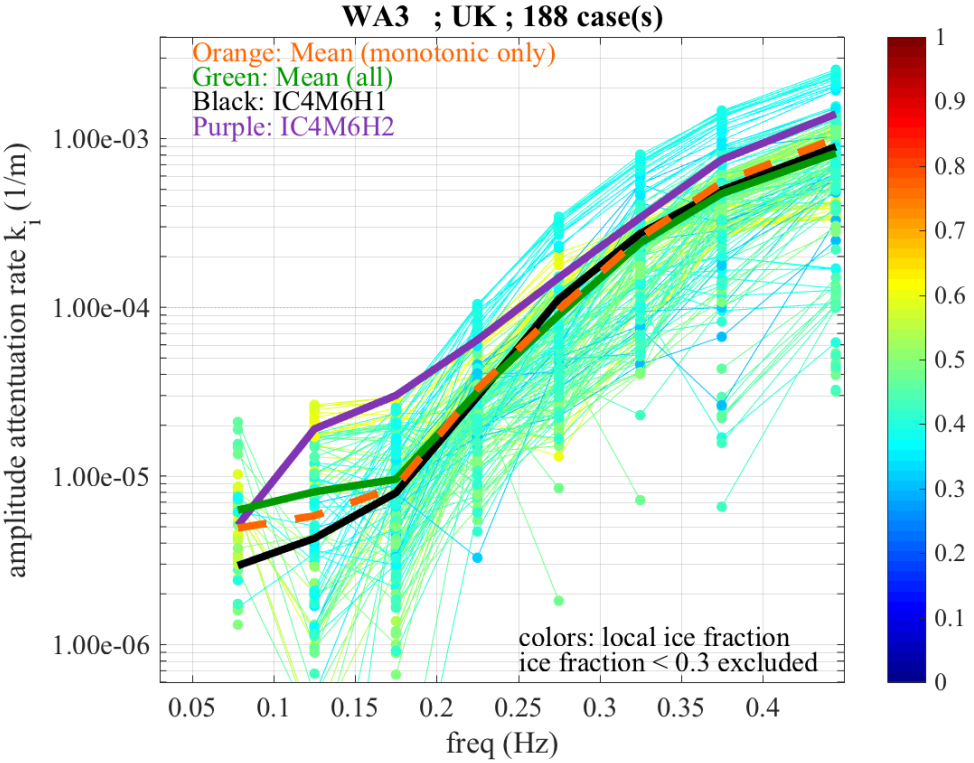

Figure 3. Like Figure 2, but using UK buoys.

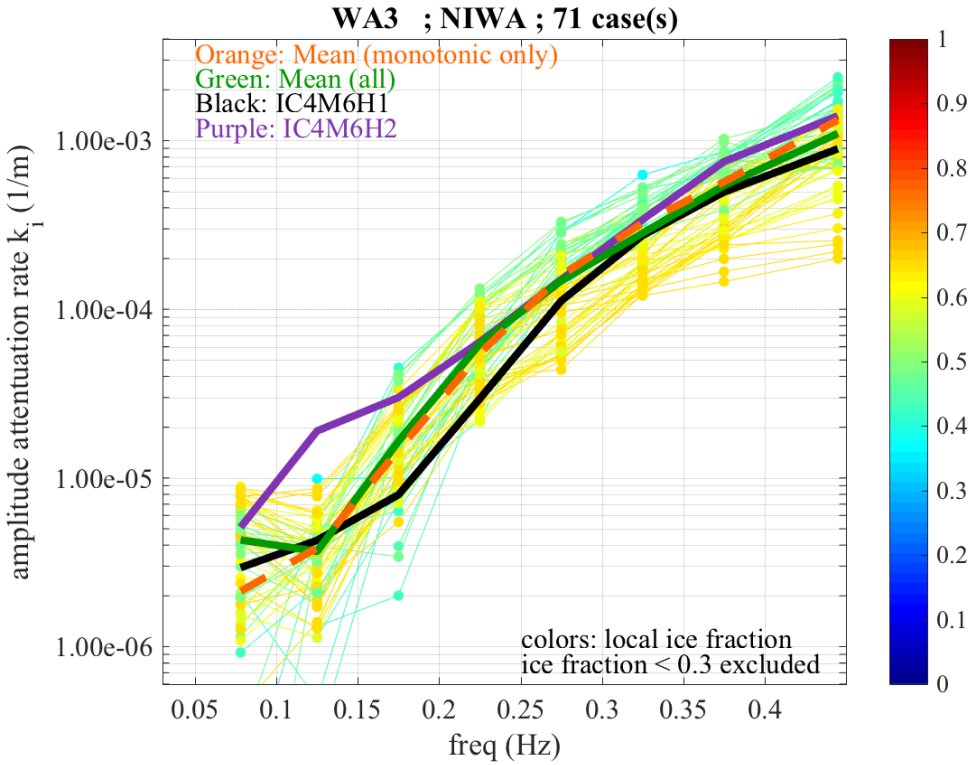

Figure 4. Like Figure 2, but using NIWA buoy.

3. Step functions created by selecting profiles based on ice photographs

3.1. Description of method

In the prior section, Figure 2 to Figure 4, individual profiles are color-scaled according to ice concentration. In the present section, we instead color-scale profiles based on the ice codes introduced in R18. These are plotted in Figure 5 to Figure 7. The R18 ice codes range from 1 (open water) to 12 (thickest frazil and pancake ice). Since only the SWIFT buoys were equipped with cameras, these plots *can only be made for the SWIFT inversion profiles*. However, the reader will notice that the number of dissipation profiles is significantly smaller than the number shown in for the SWIFT data in Figure 2 (372 profiles). At least four factors control the number of profiles plotted:

1) Cases for which the SWIFT photo was blurry or dark are excluded. The photos were blurry when ice covered the lens, and the SWIFT cameras did not have low-light capability.
2) R18 assigned ice codes to SWIFT buoys in only the southern transect of WA3. No ice codes are available for the northern transect. The SWIFT inversion profiles in Figure 2 (in Section 2) include both the northern and southern transects.
3) The number of successful inversions depends on the ice product used. The inversion provides a null solution (failure) in cases where the model outcome is insufficiently sensitive to the S_{ice} source function. This happens most often in cases where the local ice concentration is low. In case of R16, all inversions were successful because the model ice concentration (from Navy CICE) was high (often incorrectly, as discussed in R16 and R18) at all buoy locations. In case of R18, there were a significant number of failed inversions because there were significant regions which were ice-free according to the

NT2 AMSR2. In the present report, there are more successful inversions than in the inversion of the R18, since there are fewer cases of very low ice concentration in the Bootstrap fields (this report) than in the NT2 fields (R18 inversion). To prevent plotting of inversions that failed or have low confidence, in Figure 6 and Figure 7, we show only profiles from cases with at least 25% ice concentration.

4) R16 used hourly buoy data whereas R18 and the present report used half-hourly buoy data, implying twice as many spectra as R16.

Figure 5 to Figure 7 show the dissipation profiles $k_i(f)$ color-coded by ice code:

- Figure 5 from the inversion of R16;
- Figure 6 from the inversion of R18; and
- Figure 7 from the inversion of this report.

These results are averaged to create synthesized $k_i(f)$ for use in WW3 as step functions. The averaging procedure is described in Section 7. A summary is given here:

- inversion of R16 is averaged (considering ice codes, an earlier version of those shown in Figure 5) to create step function IC4M6H1, as introduced in C17
- inversion of R18 is averaged (considering ice codes shown in Figure 6) to create step function IC4M6H2, as introduced in R18
- inversion of this report is averaged as follows:
    - considering ice codes shown in Figure 7, to create step function IC4M6H3 (this Section)
    - without use of ice codes, to create step functions “WA3-SWIFT”, “WA3-UK”, and “WA3-NIWA”. See Section 4 and Figure 2 to Figure 4.

It is useful to clarify a point that may be confusing: The ice codes are *not used* in the inversion procedure. They are only used (in some cases) to present results (Figure 5 to Figure 7) or average the profiles into parametric step functions for use in WW3 (IC4M6H1, IC4M6H2, IC4M6H3).

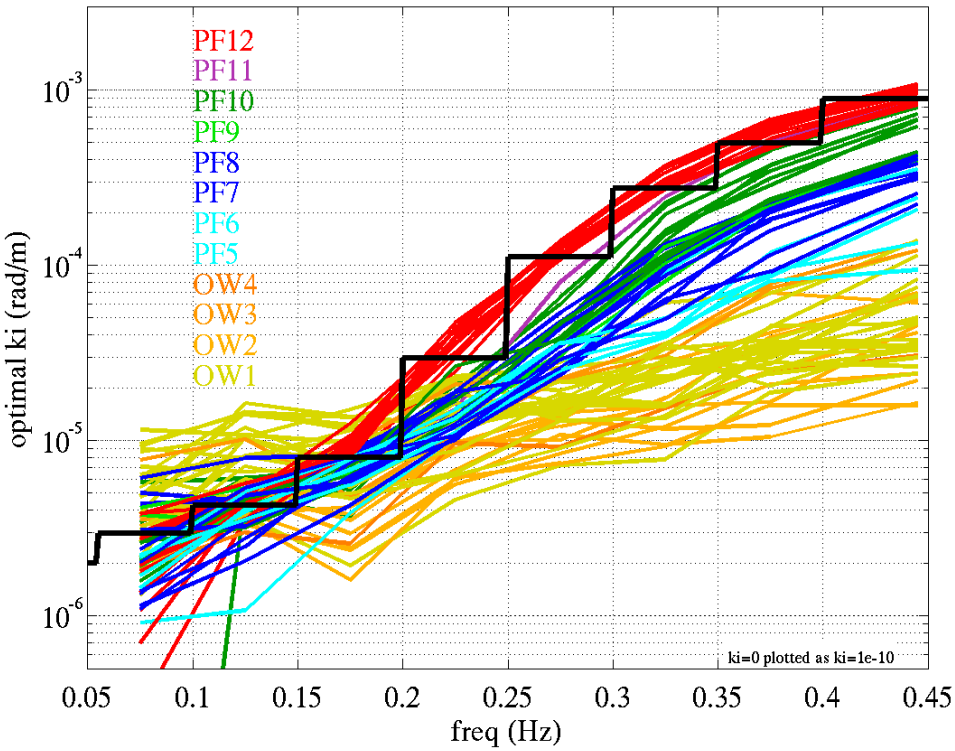

Figure 5. Dissipation profiles from the inversion of R16. Color scaling is according to ice codes as described in R18. Black step function is IC4M6H1 and is a fit to higher ice codes of R16, roughly corresponding to PF11 and PF12 here. 145 profiles are plotted here.

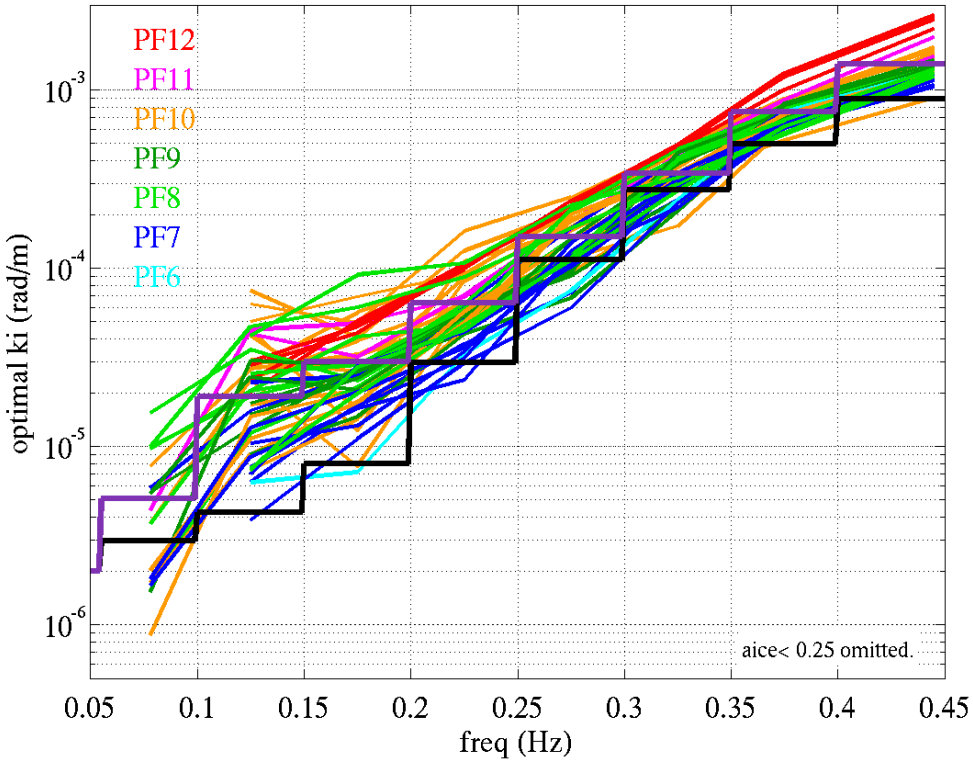

Figure 6. Like Figure 5, but the dissipation profiles are from the inversion of R18. Purple step function is IC4M6H2 and was created from the inversion profiles shown (R18). 48 profiles are plotted here.

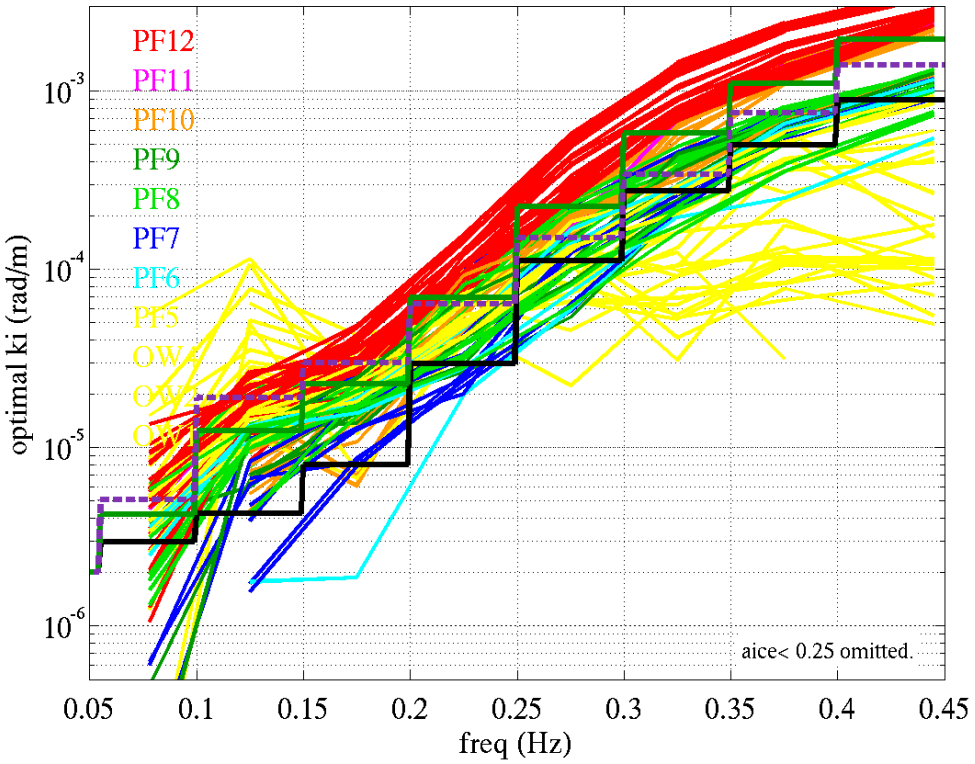

Figure 7. Like Figure 5, but the dissipation profiles are from the inversion of this report. Ice codes with values less than 6 are not used to created IC4M6H3 and are shown as yellow lines here. The green step function is IC4M6H3 and was created from the inversion profiles shown (this report). 101 profiles are plotted here.

3.2. Manual adjustment of IC4M6H2 for use in WW3

R18 states the namelist for using IC4M6H2 in WW3:

```
&SIC4 IC4METHOD = 6,
       IC4FC =   0.045   , 0.055   ,  0.10   , 0.15    , 0.20    ,
                 0.25    , 0.30    , 0.35    , 0.40    , 99.0
       IC4KI =   1.0e-6  , 2.0e-6,  5.1e-06 , 1.5e-05 , 3.0e-05,
                 6.4e-05 , 1.5e-04, 3.4e-04 , 7.5e-04 , 1.4e-03
```

The first two k_i bins here are from Ardhuin et al. (2016), and bins 3, 5, 6, 7, 8, 9, and 10 are from the R18 inversion. However, the 2nd bin from the R18 inversion was `1.9e-05`, and this was not used as the 4th bin in the namelist. Instead, it was manually adjusted to `1.5e-05` in order to provide WW3 with a smoother k_i profile. This is denoted as "IC4M6H2b" in Table 1. While this smoothing adjustment makes sense for WW3, it is antithetical to our purposes here. Therefore, in figures in this report, we use the unmodified sequence directly from the inversion. This is denoted as "IC4M6H2a" in Table 1.

3.3. Tabulated inversion results

Table 1 lists the k_i value for each of the eight coarse frequency bins from the three inversions which perform averaging using ice codes from the SWIFT cameras: IC4M6H1, IC4M6H2, and IC4M6H3. As noted in Section 3.2, IC4M6H2 has two forms: 1) IC4M6H2a, the unmodified output from averaging of the inversion profiles, and 2) IC4M6H2b which has one frequency bin manually adjusted to provide WW3 with a smoother $k_i(f)$ profile for use in the S_{ice} parameterization.

Table 1. Table of k_i values from inversion, on coarse bins. Step functions were created by selecting profiles based on ice type from SWIFT cameras.

f_{min}	f_{center}	f_{max}	IC4M6H1	IC4M6H2a	IC4M6H2b	IC4M6H3
(frequency with units Hz)			(k_i with units 1/m)			
0.056	0.078	0.100	2.94e-06	5.10e-06	5.10e-06	4.22e-06
0.100	0.125	0.150	4.27e-06	1.90e-05	1.50e-05	1.24e-05
0.150	0.175	0.200	7.95e-06	3.00e-05	3.00e-05	2.26e-05
0.200	0.225	0.250	2.95e-05	6.40e-05	6.40e-05	6.92e-05
0.250	0.275	0.300	1.12e-04	1.50e-04	1.50e-04	2.24e-04
0.300	0.325	0.350	2.74e-04	3.40e-04	3.40e-04	5.80e-04
0.350	0.375	0.400	4.95e-04	7.50e-04	7.50e-04	1.10e-03
0.400	0.445	0.490	8.94e-04	1.40e-03	1.40e-03	1.94e-03

4. Step functions created by selecting profiles based on ice concentration

In R18, individual dissipation profiles (inversion results) were presented for all cases, but average profiles were made only for cases with ice photographs. This necessarily implies that no average profiles were made using UK or NIWA buoy spectra. That is done here for the first time. The step functions are created by selecting profiles based on ice concentration, and are indicated in Figure 2 to Figure 4, alongside the results from the new inversion. The thick green line is an average of the individual inversion profiles, and the thick orange line is an average including only monotonic profiles. Rather than plotting as a step function (one step for each of the eight course frequency bins), we plot $k_i(f)$ at each of the central frequencies of the eight bins.

Since the inversion can fail for some bins and succeed for other bins (i.e. the "good bins" mentioned above), the number of valid bins varies from one spectrum to another. Thus, the averaging is done on a per-bin basis. So, for example, the 2nd (of 8) bins might be computed as an average of 200 values, whereas the 3rd bin might be computing from an average of 205 values.

These mean $k_i(f)$ profiles are for WA3 only, but analogous mean profiles could be made using the inversion results for other wave experiments. Individual profiles (i.e. before averaging) have been computed for each measured spectrum during the six of the eight wave experiments of the Sea State cruise: IS1, WA3, WA4-5, WA6, RT, and WA7, similar to Figures 79 to 89 of R18. (Also, these eight wave experiments are summarized in Section 2 of R18.)

The mean $k_i(f)$ profiles taken from only monotonic profiles (in other words, the thick orange lines in (Figure 2 to Figure 4), will be henceforth referred to as: WA3-SWIFT (Figure 2), WA3-UK (Figure 3) and WA3-NIWA (Figure 4). Table 2 lists the k_i value for each of the eight coarse frequency bins from these three inversions which perform averaging *without* using ice codes from the SWIFT cameras.

In Figure 2, we see that WA3-SWIFT (orange line) is similar to IC4M6H2 (purple line) from the R18 inversion, though WA3-SWIFT is a bit steeper in frequency space. The similarity is unsurprising, given that both IC4M6H2 and WA3-SWIFT are based on inversion using SWIFT data and WW3 forced by AMSR2. Differences between the IC4M6H2 and WA3-SWIFT inversions (which cause the difference in profile slope) are summarized in Section 7.

Table 2. Table of k_i values from inversion, on coarse bins. Step functions were created by selecting profiles based on ice concentration.

f_{min}	f_{center}	f_{max}	WA3-SWIFT	WA3-Doble	WA3-NIWA
(frequency with units Hz)			(k_i with units 1/m)		
0.056	0.078	0.100	4.48e-06	4.92e-06	2.13e-06
0.100	0.125	0.150	1.12e-05	5.80e-06	3.86e-06
0.150	0.175	0.200	2.28e-05	8.62e-06	1.46e-05
0.200	0.225	0.250	6.91e-05	3.28e-05	5.47e-05
0.250	0.275	0.300	2.06e-04	9.70e-05	1.59e-04
0.300	0.325	0.350	5.08e-04	2.59e-04	3.25e-04
0.350	0.375	0.400	9.33e-04	5.51e-04	5.68e-04
0.400	0.445	0.490	1.69e-03	1.00e-03	1.32e-03

5. Binomial fits to step functions

Recognizing that some readers will find it more convenient to compare to our results using polynomial fit rather than step functions, we performed a fit to our step functions. This is shown in Figure 8, in the form of $k_i = c_2 f^2 + c_4 f^4$. Note that the coefficients are dimensional; non-dimensionalization is discussed in R18.

Fits are based on least squares, using $\log_{10}(k_i)$ so as to not unduly weight the high values. RMSE, with "errors" being the differences in $\log_{10}(k_i)$, are indicated in text in Figure 8. Of the six fits, the IC4M6H2 points are best matched using this binomial.

Our use of the binomial $c_2 f^2 + c_4 f^4$ follows M14, who have: $\alpha = 2k_i = c_{2,\propto} f^2 + c_{4,\propto} f^4$ with $c_{2,\propto}$=2.12e-3 and $c_{4,\propto}$=4.59e-2. Thus, their $c_2 = 1.06$e-3 and $c_4 = 2.30$e-2 (dividing by two since their equation is for α and ours is for k_i). This means that their c_2 is about twice that of IC4M6H2, while their c_4 is close to that of IC4M6H2. Higher coefficients are expected in the M14 case, given the more substantial ice cover. All c_2 and c_4 values, including those from M14, are listed in Table 3.

Because of the difference in c_2, and similarity in c_4 relative to Meylan (2014), we postulate that the ice thickness affects the behavior of the f^2 while the f^4 term is insensitive to ice thickness. However, the generally higher values of Doble et al. (2015), compared in Section 6, indicates that we should be cautious with this interpretation.

For WW3 users, this binomial can be activated via IC4M2 (C17). That implementation uses the form $\alpha = c_{2,\propto} f^2 + c_{4,\propto} f^4$, so coefficients herein should be multiplied by two: $c_{2,\propto} = 2c_2$ and $c_{4,\propto} = 2c_4$.

In R18, the analysis of the slope $\partial k_i(f)/\partial f$ suggests that a binomial $\alpha = c_2 f^2 + c_{4.5} f^{4.5}$ or $\alpha = c_2 f^2 + c_5 f^5$ would match the inversion results as well as (or better than) $\alpha = c_2 f^2 + c_4 f^4$. We use the $\alpha = c_2 f^2 + c_4 f^4$ form here only because it allows direct comparison to M14.

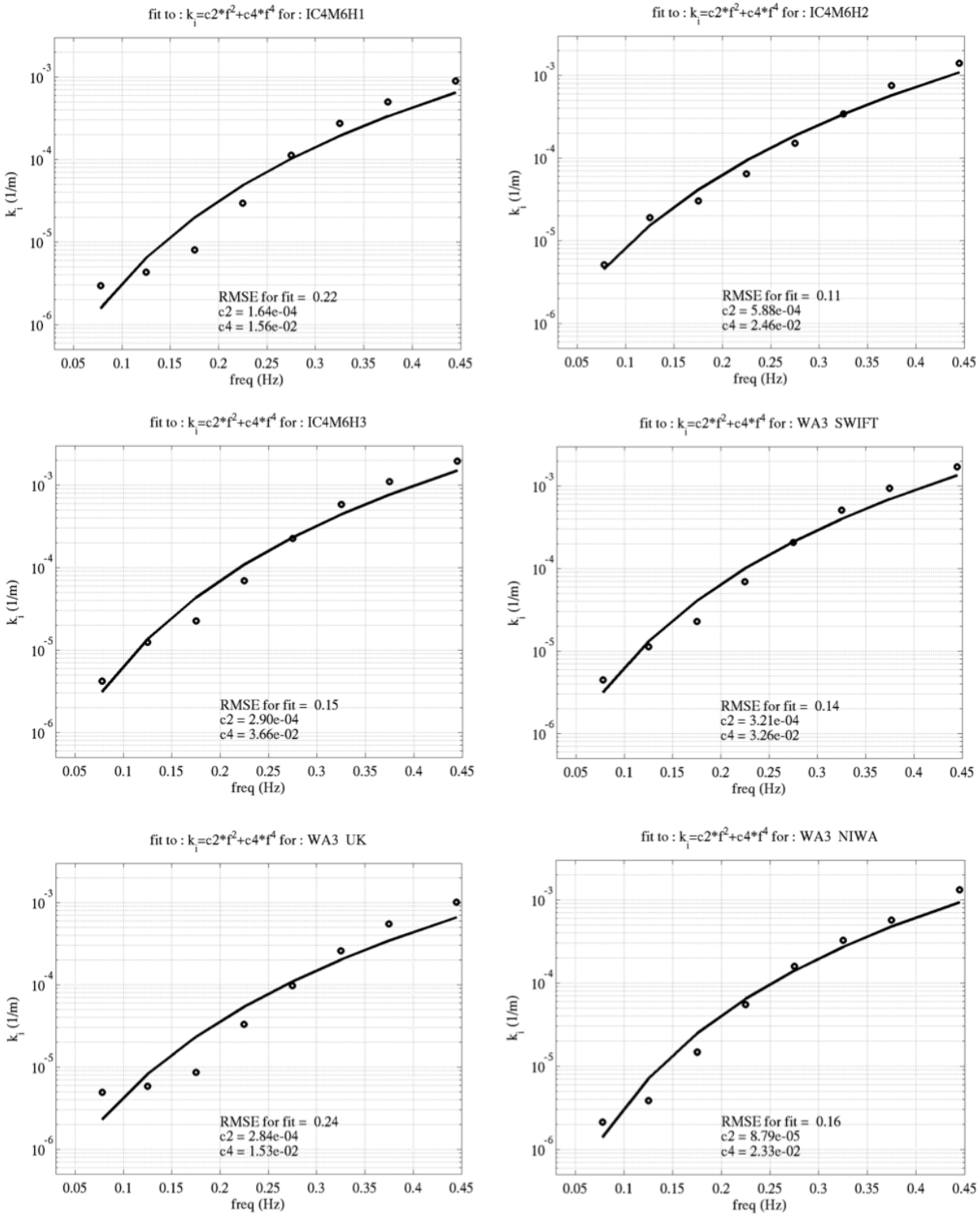

Figure 8. Binomial fits to our six step functions, in the form of $k_i = c_2 f^2 + c_4 f^4$. Center frequency of each step is plotted with a circle (eight steps for the eight coarse frequency bins).

Table 3. Table of c_2 and c_4 values for binomial $k_i = c_2 f^2 + c_4 f^4$.

name	c_2	c_4
IC4M6H1	1.64e-04	1.56e-02
IC4M6H2	5.88e-04	2.46e-02
IC4M6H3	2.90e-04	3.66e-02
WA3 SWIFT	3.21e-04	3.26e-02
WA3 UK	2.84e-04	1.53e-02
WA3 NIWA	8.79e-05	2.33e-02
Meylan et al. (2014)	1.06e-03	2.30e-02

The binomial fitting allows us to include all seven $k_i(f)$ profiles on the same plot: this is Figure 9. Of our six profiles, there is an apparent separation into two groups: a higher group (IC4M6H2, IC4M6H3, WA3-SWIFT) and a lower group (IC4M6H1, WA3-UK, WA3-NIWA). It is unsurprising that IC4M6H2, IC4M6H3, WA3-SWIFT are grouped together, since all are using SWIFT data. It is less intuitive that IC4M6H1, which is also using SWIFT data, falls into the other group. However, this has a simple explanation. In IC4M6H1, two effects are counteracting each other: 1) overprediction of ice concentration (which makes k_i small) and 2) buoy spectra that are relatively weak (which makes k_i large). The fact that IC4M6H1 falls in the "lower grouping" also explains why it matched UK and NIWA buoys very well for WA3 in R18: this was purely serendipitous, recalling that R18 use improved (lower) ice concentration, and the UK (and probably NIWA) buoys have relatively energetic spectra.

The reference to "weak" and "energetic" spectra may seem cryptic to readers that are not familiar with the WA3 spectra. The issue (and possible causes) was discussed in Section 6.3.6 of R18. In short: the UK buoy spectra appear to be more energetic than the SWIFT buoy spectra, even when placed nearby. The outcome is that the WW3 hindcasts tended to have a negative bias in significant waveheight (SWH) when compared to UK buoys and positive bias when compared to SWIFT buoys. The model had negative bias relative to the NIWA buoy, suggesting a similarity between the NIWA buoy and UK buoys, but this similarity is not certain, as the NIWA buoy was north of the main (southern) transect.

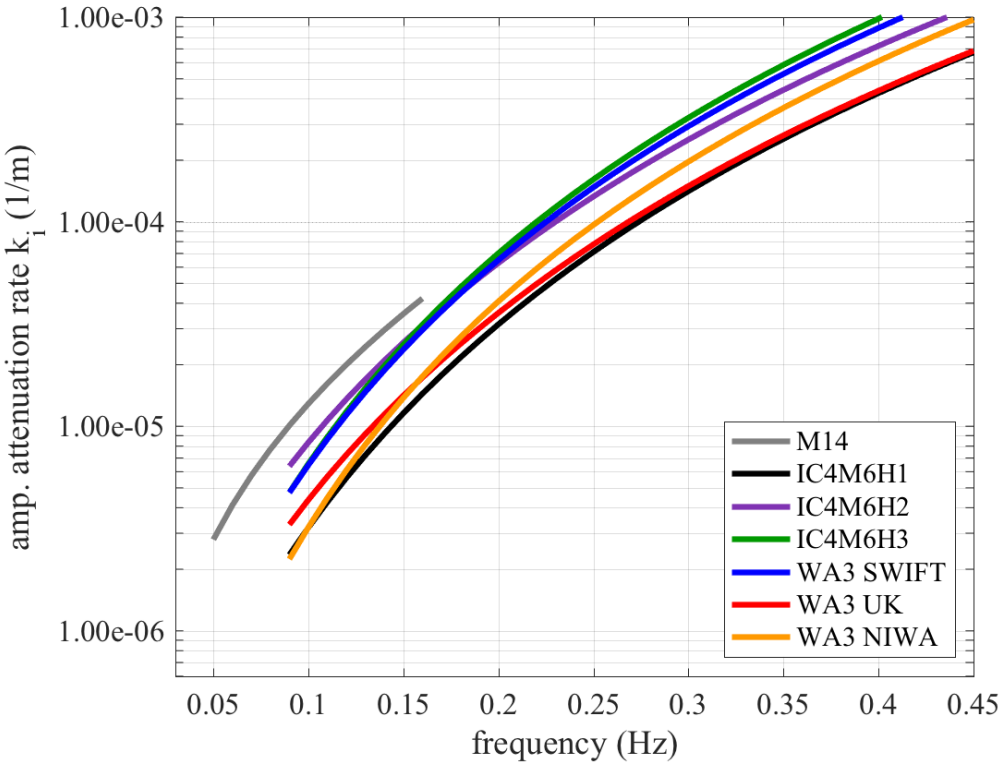

Figure 9. Comparison of seven binomial functions of the form following Meylan et al. (2014), $k_i = c_2 f^2 + c_4 f^4$.

6. Comparisons to other datasets

6.1. Graphical comparison

Figure 10 compares four of the binomials against additional historical datasets (Wadhams et al. (1988), Ardhuin et al. (2016), and Doble et al. (2015)). The Wadhams et al. (1988) dataset is based on instrumentation on very thick floes. This thickness makes the large dissipation rates unsurprising. Further, according to Meylan et al. (2018), errors may be larger than normal, because measurements were not made simultaneously. The high dissipation rates reported by Doble et al. (2015) (in larger pancakes near Antarctica) are more difficult to explain. It is intuitive that they are higher than those for WA3 here (smaller pancakes in the Arctic), but we do not know why these measurements would show more dissipation than M14 (broken floes near Antarctica). We assert that the WA3 measurements, because of the careful deployment of the buoys, can be considered as the most reliable of all the results.

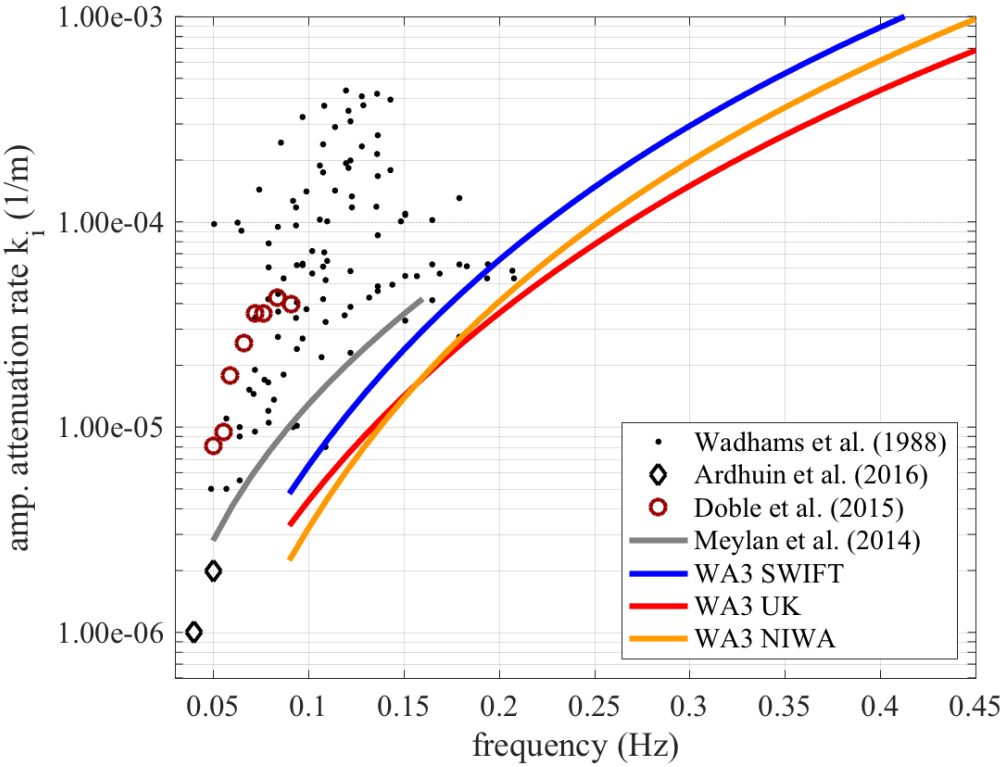

Figure 10. Comparison of new binomial functions (based on WA3 SWIFT, WA3 UK, and WA3 NIWA) against four historical datasets.

6.2. Slope dependence

R18 provide an inventory of the slope dependence, $k_i \propto f^n$. That inventory is repeated here:

- Ardhuin boundary layer model for friction at the ice-water interface, also known as the basal friction model for IC2, from analysis of Figure 94 in R18:
  - turbulent regime: $n = 3$
  - laminar regime: $n = 3.5$
- Kohout et al. (2011) model for friction at the ice-water interface, based on drag formula: $dE/dt = \tau u_{max} = \rho C_d u_{max}^3$. This gives $n = 4$.

- Keller (1998) viscous layer model (full dispersion relation), from analysis of Figure 101 in R18: This gives $n = 7$. This number is independently confirmed by M18. The Wang and Shen (2010) model, implemented in WW3 as IC3, reduces to the Keller model for cases of zero elasticity. Inclusion of elasticity in IC3 has a large impact on $k_i(f)$ (see R16 and Cheng et al. 2017), so it is not possible to ascribe a value for n to IC3 in its viscoelastic form.
- In Lamb (1932), Article 349, which is on "the effect of viscosity on water waves", there is an estimate for dissipation by viscosity in the entire water column. See also Weber (1987) and Sutherland et al. (2017). Thisgives $n = 5$.
- In Lamb (1932) Article 351, on the "calming effect of oil on waves". This employs the concept of Stokes boundary layer thickness for the case of an "inextensible surface cover"[3]. It gives $n = 3.5$. See also Weber (1987) and Sutherland et al. (2017).
- Meylan et al. (2014). This is an empirical polynomial fit. It suggests two regimes (so binomial): $n = 2$ and $n = 4$.
- IC4M6H2 in R18. Like Meylan et al. (2014), this gives two regimes: $n = 2$ and $n = 4$ to 5. This slope analysis is in Section 6.2.5 of R18.

In this list, only the Keller model has explicit dependence on ice thickness, though observational studies such as Doble et al. (2015) and R16 find a dependence of dissipation on ice thickness.

M18 include additional models:

- The Greenhill (1887) model for a thin elastic plate, with viscosity added. M18 call this the viscous Greenhill model. They find that it has $n = 11$. Mosig et al. (2015) present a related model, which they denote as "FS". This is the Fox and Squire (1994) model, modified (or extended) to include viscosity and reduced by one dimension to allow more direct comparison to the Wang and Shen (2010) model in that paper. This makes it a thin beam model rather than a thin plate model. The FS model, unlike the simpler Greenhill model, has a complex-valued shear modulus. A final, related model is the one implemented in WW3 as "IC5", which is the Fox and Squire (1994) model, again modified (or extended) to include viscosity, but without reduction of dimension. Thus, IC5 is a viscoelastic thin plate model, comparable to the viscous Greenhill model described in M18. We refer to this grouping of viscoelastic beam or plate models as "EFS models".
- The Robinson and Palmer (1990) model for a thin viscoelastic plate is found by M18 to have $n = 3$. A related model is the "RP" model used in Mosig et al. (2015) which is the Robinson and Palmer (1990) model, reduced by one dimension. Thus, both the FS and RP models in Mosig et al. (2015) are thin beam models.
- M18 also propose two new models, with different assumptions about the cause of dissipation:
    - Dissipation is associated with the product of pressure and velocity: $n = 2$.

[3] The idea here is that the film (or ice cover) moves vertically but not horizontally with the wave orbits. Thus, the water is sliding/slipping under the film. However, it is not a "free slip", and since there is viscosity in the water, a boundary layer develops, which results in dissipation. Lamb (1932) include a disclaimer: that this mechanism only works for cases where the wavelength is "sufficiently small". We do not feel that it is useful for cases of long waves and loose ice (e.g. pancakes).

- Dissipation is associated with the product of ice thickness and the square of horizontal velocity: $n = 3$.

This inventory can be expanded by including additional models and empirical studies. The comparison is particularly interesting because it suggests possible physical explanations (via the models) for the observed/empirical values of n. For example, the $n = 4$ portion of the M14 and IC4M6H2 binomials may be associated with friction at the ice-water interface.

7. Summary of differences between the step functions

Here, we summarize the differences between methods used to generate the step functions. All step functions here are based on WA3.

IC4M6H1

- Based on inversion of R16; referred to as "IC4M6H" in C17 and R18
- Wind forcing from NAVGEM, 0.5° resolution
- Air-sea temperature differences are not used to modify drag: this corresponds to the "STAB0" switch in WW3 and is the most common way to operate WW3 (e.g. taking examples from U.S. Navy, NCEP, and Ifremer).
- $\beta_{max} = 1.52$ (controls the strength of wind input source function in ST4 physics)
- Inner WW3 grid is relatively coarse: 10 km resolution, described in R16
- Ice concentration is from Navy CICE as described in R16
- Step function is first given in C17 and is made by averaging all "P/FR-H" $k_i(f)$ profiles from Figure 9 of R16 (shown as red lines in that figure). Results for cases without valid ice codes are not used in the creation of the step function.
- Buoy data is the hourly dataset made available shortly after the cruise

IC4M6H2

- Described in R18.
- Inner WW3 grid is of finer resolution than prior: 5 km resolution, described in C17 and R18
- $\beta_{max} = 1.2$
- Ice concentration is from the high temporal resolution AMSR2 fields, processed using NT2 algorithm as described in R18.
- Step function is based on the average of $k_i(f)$ profiles which correspond to cases of ice concentration a_{ice} greater than 0.25. This has the side-effect of excluding all cases with ice code (from SWIFT camera, see R18) of less than 6. Thus, it was not necessary to impose any exclusion based on ice code. The $k_i(f)$ bins which did not satisfy monotonicity were excluded; this only affected the outcome for the 2nd frequency bin. Results for cases without valid ice codes are not used in the creation of the step function.
- Buoy data is the reprocessed half-hourly spectra.
- Otherwise, similar to IC4M6H1

IC4M6H3

- Introduced in this report.
- There are three differences associated with changes to the WW3 simulations, as described in Section 2:
  1) Wind forcing from NAVGEM, 0.28° resolution.

2) Air-sea temperature differences are used to modify drag. This corresponds to the "STAB3" switch in WW3 and is a less common way to operate WW3 (it is used by UK Met Office, in conjunction with ST3).
3) Ice concentration is processed using the Bootstrap algorithm.

- As with IC4M6H2, the step function is based on averaging the $k_i(f)$ profiles which correspond to cases of ice concentration, a_{ice}, greater than 0.25. However, since a_{ice} is different, we actually have 24 cases with a_{ice} greater than 0.25 and ice code less than 6. Therefore, to be consistent with ice codes used in IC4M6H2, we added an exclusion for ice codes less than 6. Results for cases without valid ice codes are not used in creation of the step function.
- Otherwise, similar to IC4M6H2.

WA3-SWIFT

- Here, we include cases without any discrimination based on the quality of ice observations from the SWIFT cameras. Thus, it includes cases of darkness or obscured lens, e.g. when the buoy was encased in ice. This contrasts with the step function of IC4M6H3.
- Step function is based on averaging the $k_i(f)$ profiles which correspond to cases of ice concentration a_{ice} greater than 0.30.
- Any $k_i(f)$ profiles that were not fully monotonic were excluded from the averaging. The outcome of this is indicated in Figure 2 by showing the mean profile with and without this exclusion.
- Any $k_i(f)$ profile which did not have at least four "good bins" was excluded. In case of WA-SWIFT, this meant the exclusion of 16 out of 388 $k_i(f)$ profiles. A "good bin" here refers to a bin for which the inversion procedure found a solution. Examples of failed inversions are given in R18.
- Otherwise, it is similar to IC4M6H3.

WA3-UK

- Uses UK buoys. Cameras were not installed on these buoys.
- Otherwise, similar to WA3-SWIFT

WA3-NIWA

- Uses the NIWA buoy. A camera was not installed on this buoy.
- Otherwise, similar to WA3-SWIFT

8. Discussion

8.1. Power dependence

The primary challenge in modeling wave attenuation by ice is that the mechanism for energy removal from the waves is unknown. Measurements of wave attenuation in ice are the primary means of solving this problem, but they do not in any way measure the actual mechanism, and the mechanism must therefore be inferred.

Wave dissipation is strongly dependent on frequency. In M18, multiple datasets of wave attenuation measurements were analyzed with a focus on this dependence. Measurements suggest variable power law behavior with a coefficient between two and four ($2 \leq n \leq 4$). This

multiple power law implies that there are two different mechanisms removing energy which dominated for either long or short waves. The obvious question is what mechanism could lead to these power laws.

To try and resolve this question, M18 analyzed wave measurements and various wave attenuation models. Some of these attenuation models are very complex and to reduce this complexity it was assumed that, as observed in field data, the real part of the wavenumber is not substantially changed by a thin ice layer. This small change implies that the ice effect is second order. If this assumption was violated, we would expect the ice to attenuate the wave energy very rapidly as the interaction between the waves and ice would be dominant. By making this assumption of a small change to the real part of the wavenumber, the dispersion equations were solved using a perturbation method. This resulted in power dependencies from $n = 2$ to $n = 11$. Our model-data inversions for WA3 do not support $n > 5$. This implies that hindcasts of this case using the Keller model ($n = 7$) or EFS model ($n = 11$) will perform poorly. Looking beyond the WW3 context, we can conclude that either the physical mechanisms used in these models were not major factors in the WA3 case, and/or underlying assumptions of the models are inappropriate for that case.

Nonlinearity (i.e. dependence of k_i on wave amplitude) is not considered in our discussion of power relations ($k_i \propto f^n$). It is understood that nonlinearity severely complicates the creation of parametric models from observational results, and it is a possible explanation for discrepancies, e.g. WA3 vs. M14 vs. Doble et al. (2015). It is a daunting task to map the dependency of k_i on three independent variables (frequency, ice type, and wave amplitude) using field studies. The reader is referred to Squire (2018) for detailed discussion.

8.2. Application to hindcasts

Forward modeling, i.e. hindcasting, is not included in this report. The Bootstrap AMSR2 fields have been applied in hindcasts for the entire Sea State cruise using the IC4M6H1 S_{ice}, and are compared to Synthetic Aperture Radar in Gemmrich et al. (in review), but the model results are not sufficiently different from the same hindcast using NT2 AMSR2 to justify a new, comprehensive validation against buoy data here. The reader is referred to R18 and Sutherland et al. (2018) for validations of the model using NT2 forcing.

The WA3-SWIFT, WA3-UK, and WA3-NIWA step functions have not been applied to hindcasts at time of writing. However, given the similarity between IC4M6H1, WA3-UK, and WA3-NIWA mean profiles, we can expect that any hindcasts with the latter two (or the binomial fits of the same) would behave in similar fashion to the hindcasts with IC4M6H1 in R18.

8.3. Impact of sea ice on C_g

The step functions and binomial fits created here only apply to dissipation, $k_i(f)$, and do not address the impact of sea ice on the real part of the wavenumber, $k_r(f)$. These are implemented as IC4 in WW3 (see C17). The Wang and Shen model is implemented as IC3 in WW3 (see WW3DG (2016) and Cheng et al. (2017)), and this model does address both parts of the complex wavenumber via solution of a dispersion relation. In the case of WA3, the observed modification of $k_r(f)$ by sea ice was negligible for frequencies below 0.3 Hz and small for frequencies between 0.3 Hz and 0.5 Hz (Collins et al. 2018). Though this may be a common outcome in a

MIZ with loose sea ice, we cannot assume that this is a general rule. Liu and Mollo-Christensen (1988) argue that the impact on C_g can be significant within the ice pack, where the sea ice is in compression.

The modification of $k_r(f)$ by sea ice can, in principle, produce effects analogous to refraction, shoaling and de-shoaling by bathymetry. Such effects are still rather academic and not included in forecast models. One reason for the latter is the potential for sea ice to increase the group velocity C_g dramatically, forcing a major reduction in time step to avoid Courant instability, which in turn would make a model much more expensive.

A less obvious role is one that we have not discussed previously. By tradition, dissipation by sea ice is quantified by the exponential decay rate of amplitude or energy via k_i or α, respectively. In WW3, we convert this to time domain as $D_{ice} = S_{ice}/E = -2C_g k_i = -C_g \alpha$ (e.g. Rogers and Orzech 2013). In these wave-ice and wave-mud dispersion relations, much of the frequency variation is introduced via the modification of C_g. For example, according to Prof. Hayley Shen (personal communication), with the Liu and Mollo-Christensen (1988) model, implemented in WW3 as IC2, $k_i(f)$ is non-monotonic while $D_{ice}(f)$ is monotonic, because of the shape of $C_g(f)$. The non-monotonicity is sometimes referred to as "roll-over" in this context. The reader is referred to Li et al. (2017) for a detailed review of roll-over.

9. Summary and conclusions

9.1. Summary

Here we focus on one wave experiment, Wave Array #3 (WA3) of the Sea State cruise. The model-data inversion (to create distribution of dissipation rate as a function of frequency) of R18 is repeated using ice concentration from the AMSR2 instrument processed using the "Bootstrap" algorithm. The resulting distributions (or profiles) are averaged, using groupings by buoy type, ice type, and ice concentration. Averaging requires subjective criteria, e.g. whether to include non-monotonic $k_i(f)$ profiles. Tabulated values of $k_i(f)$ are presented which can be used as step functions in WW3 for computations of the source function for dissipation by sea ice, S_{ice}.

The average profiles are fitted to polynomials following Meylan (2014) and compared to other data and average profiles from the literature. The binomial fits are provided, which can also be used as instructions for WW3 to calculate S_{ice}. Since the binomial fits consist of only two numbers, they are easily usable by other researchers for comparison to existing and future datasets.

We review the power-law relations, $k_i \propto f^n$ given in both observational and theoretical studies. We list a total of 12 values of n, ranging from 2 to 11 (see Section 6.2).

9.2. Conclusions

Conclusions are as follows:

- Since the Bootstrap AMSR2 fields have non-zero ice concentration over a larger area (relative to NT2 AMSR2), the inversion with the former yields a larger number of valid solutions for dissipation profiles, $k_i(f)$.

- Our $k_i(f)$ profiles (from pancake ice in the Arctic) are generally lower than those of M14 (broken floes near Antarctica) and Doble et al. (2015) (pancake ice near Antarctica).
- Regarding the fitting to binomials, $k_i = c_2 f^2 + c_4 f^4$: all fittings yield c_2 (controlling low frequency dissipation) smaller than that of M14, which is unsurprising given the more substantial ice in the M14 case. Some fittings yield c_4 (controlling higher frequency dissipation) very close to that of M14.
- We hypothesize that the two terms in the binomials correspond to two distinct physical processes. The inventory of power relations given in Section 6.2 provides clues for these physical processes, i.e. which ones are candidates and which ones cannot be candidates.
- We hypothesize that the similar c_4 in W14 (broken floes near Antarctica) and Sea State WA3 (pancake ice in the Arctic) indicates a common physical process. However, it is difficult to reconcile with the high dissipation rates observed in Doble et al. (2015) (pancake ice near Antarctica).
- The $k_i(f)$ dissipation profiles from model/data inversion using UK and NIWA buoys are lower than comparable profiles using SWIFT buoys. This is a result of discrepancies in the buoy observations themselves (SWIFT spectra are lower than spectra from nearby UK buoys). We make no assertions regarding the superiority of one dataset over another, but it is important to be aware of the implied uncertainty.

9.3. Outlook

- Our list of power-law relations is not comprehensive. We recommend that it be expanded, since it facilitates interpretation of observational results, as noted above.
- It is a daunting task to map the dependency of k_i on three or more independent variables (frequency, ice conditions, and wave amplitude) using field studies. Nevertheless, we should work further to exploit existing observational data, and new field experiments should be conducted. Parallel to this, theoretical and process modeling studies should attempt to reconcile and bridge these data.

Acknowledgments

We thank Jim Thomson, Joe Talbert, Alex DeKlerk, Madison Smith (U. Washington/APL), Martin Doble (Polar Scientific Ltd.), and Peter Wadhams (Cambridge U.) for their substantial labors building, preparing, maintaining, deploying and recovering the wave buoys, and for the processing and management of the associated data. Dr. Li Li (NRL-DC) processed the AMSR2 data, used as input to WW3 during the model-data inversion.

This is NRL contribution number NRL/MM/7320-18-3997 and is approved for public release.

References

Ardhuin, F., P. Sutherland, M. Doble, and P. Wadhams (2016). Ocean waves across the Arctic: Attenuation due to dissipation dominates over scattering for periods longer than 19 s, *Geophys. Res. Lett.,* **43**, 5775–5783, doi:10.1002/2016GL068204.

Cheng, S., W.E. Rogers, J. Thomson, M. Smith, M.J. Doble, P. Wadhams, A.L. Kohout, B. Lund, O.P.G. Persson, C.O. Collins III, S.F. Ackley, F. Montiel, and H.H. Shen (2017). Calibrating a Viscoelastic Sea Ice Model for Wave Propagation in the Arctic Fall Marginal Ice Zone. *J. Geophys. Res.,* **122** doi://10.1002/2017JC013275

Collins, C.O., and W.E. Rogers (2017). A Source Term for Wave Attenuation by Sea ice in WAVEWATCH III ®: IC4, NRL Report NRL/MR/7320--17-9726, 25 pp. [available from www7320.nrlssc.navy.mil/pubs.php].

Collins, C., M. Doble, B. Lund, and M. Smith (2018). Observations of surface wave dispersion in the marginal ice zone. *J. Geophys. Res.,* **123**. doi:10.1029/2018JC01378.

Comiso, J.C., D.J. Cavalieri, T. Markus (2003). Sea Ice Concentration, Ice Temperature, and Snow Depth Using AMSR-E Data. *IEEE Transactions on Geoscience and Remote Sensing*, **41**(2), 243-252.

Doble, M. J., G. De Carolis, M. H. Meylan, J.-R. Bidlot, and P. Wadhams (2015). Relating wave attenuation to pancake ice thickness, using field measurements and model results, *Geophys. Res. Lett.,* **42**, 4473–4481, doi:10.1002/2015GL063628.

Fox, C., and V. A. Squire (1994). On the oblique reflexion and transmission of ocean waves at shore fast sea ice, *Philos. Trans. R. Soc. London A*, **347** (1682), 185–218, doi:10.1098/rsta.1994.0044.

Hogan, T., and 16 Coauthors (2014). The Navy Global Environmental Model, *Oceanography, 27(3),* 116-125.

Keller, J.B. (1998). Gravity waves on ice-covered water. *J. Geophy. Res.*, **103** (C4): 7663-7669.

Kohout, A. L., M. H. Meylan, D. R. Plew (2011). Wave attenuation in a marginal ice zone due to the bottom roughness of ice floes. *Annals of Glaciology*, **52**(57), 118-122.

Kohout, A. L., B. Penrose, S. Penrose, M.J.M. Williams (2015). A device for measuring wave-induced motion of ice floes in the Antarctic marginal ice zone. *Annals of Glaciology,* **56** (69), 415-424.

Gemmrich, J., W.E. Rogers, J. Thomson, S. Lehner (in review). Wave evolution in off-ice wind conditions.

Lamb, H. (1932). *Hydrodynamics*. Sixth Edition. New York, Dover Publications.

Li, J., Kohout, A. L., Doble, M. J., Wadhams, P., Guan, C., and Shen, H. H. (2017). Rollover of apparent wave attenuation in ice covered seas. *J. Geophy. Res.*, **122**. https://doi.org/10.1002/2017JC012978.

Liu, A.K. and E. Mollo-Christensen (1988). Wave propagation in a solid ice pack. *J. Phys. Oceanogr.*, **18**, 1702-1712.

Markus, T., and D.J. Cavalieri (2000). An enhancement of the NASA Team sea ice algorithm. *IEEE Trans. Geosci. Rem. Sens*., **38**(3), 1387-1398.

Markus, T., and D.J. Cavalieri (2009). The AMSR-E NT2 sea ice concentration algorithm: its basis and implementation. *J. Rem. Sens. Japan*, **29**(1), 216-225.

Meylan, M., L. G. Bennetts, and A. L. Kohout (2014). In situ measurements and analysis of ocean waves in the Antarctic marginal ice zone, *Geophys. Res. Lett.*, **41**, 5046–5051, doi:10.1002/2014GL060809.

Meylan, M.H., L.G. Bennetts, J.E.M. Mosig, , W.E. Rogers, M.J. Doble, M.A. Peter, (2018). Dispersion relations, power laws, and energy loss for waves in the marginal ice zone. *J. Geophys. Res. Oceans*, **123**. doi:10.1002/2018JC013776.

Mosig, J. E. M., F. Montiel, and V. A. Squire (2015). Comparison of viscoelastic-type models for ocean wave attenuation in ice-covered seas, *J. Geophys. Res.*, **120**, 6072–6090, doi:10.1002/2015JC010881.

Robinson, N. J., and S. C. Palmer (1990). A modal analysis of a rectangular plate floating on an incompressible liquid, *J. Sound Vibration*, **142**(3), 453–460, doi:10.1016/0022-460X(90)90661-I.

Rogers, W. E., and M. D. Orzech (2013). *Implementation and testing of ice and mud source functions in WAVEWATCH III®*, NRL Memorandum Report, NRL/MR/7320-13-9462, 31 pp.

Rogers, W.E., J. Thomson, H.H. Shen, M.J. Doble, P. Wadhams and S. Cheng (2016). Dissipation of wind waves by pancake and frazil ice in the autumn Beaufort Sea, *J. Geophys. Res.*, **121,** 7991-8007, doi:10.1002/2016JC012251.

Rogers, W.E., P. Posey, L. Li, R.A. Allard (2018). Forecasting and hindcasting waves in and near the marginal ice zone: Wave modeling and the ONR "Sea State" field experiment, NRL Report NRL/MR/7320--18-9786, 179 pp. [available from www7320.nrlssc.navy.mil/pubs.php].

Sutherland, G., T. Halsne, J. Rabault, A. Jensen (2017). The attenuation of monochromatic surface waves due to the presence of an inextensible cover. *Wave motion*, **68**, 88-96.

Sutherland, P., J. Brozena, W.E. Rogers, M. Doble, P. Wadhams (2018). Airborne remote sensing of wave propagation in the marginal ice zone, *J. Geophys. Res.* (Advance online publication), doi:10.1029/2018JC013785.

Squire, V.A. (2018). A fresh look at how ocean waves and sea ice interact, *Phil. Trans. A*. (Advance online publication), 13 pp.

Thomson, J. (2012). Wave breaking dissipation observed with SWIFT drifters, *J. Atmos. Ocean. Tech.,* **29**, 1866–1882, doi:10.1175/JTECH-D-12-00018.1.

Thomson, J. (2015). ONR Sea State DRI Cruise Report: R/V Sikuliaq, Fall 2015 (SKQ201512S), 45 pp. retrieved from http://www.apl.washington.edu/project/project.php?id=arctic_sea_state on Aug. 9 2016. 45 pp.

Thomson, J., and W. E. Rogers (2014). Swell and sea in the emerging Arctic Ocean, *Geophys. Res. Lett*., **41**, doi:10.1002/2014GL059983.

Thomson, J., and 27 co-authors (2016). Emerging trends in the sea state of the Beaufort and Chukchi seas, *Ocean Modeling*, **105**, 1-12, doi:10.1016/j.ocemod.2016.02.009.

Thomson, J., and 32 co-authors, Overview of the Arctic Sea State and Boundary Layer Physics Program, *J. Geophys. Res. Oceans* (Advance online publication) doi:10.1002/2018JC013766.

Tolman, H. L. (1991). A Third-generation model for wind-waves on slowly varying, unsteady, and inhomogeneous depths and currents, *J. Phys. Oceanogr.* **21**(6*),* 782-797.
Tolman, H. L. (2003). Treatment of unresolved islands and ice in wind wave models, *Ocean Modelling,* **5**, 219-231.
Tolman, H.L. (2009) User Manual and System Documentation of WAVEWATCH III^{TM} Version 3.14, Tech. Note, NOAA/NWS/NCEP/MMAB, 220 pp.
Tolman, H. L. and the WAVEWATCH III® Development Group (2014). *User Manual and System Documentation of WAVEWATCH III® version 4.18*, *Tech. Note 316, NOAA/NWS/NCEP/MMAB*, 282 pp. + Appendices.
Wadhams, P., V. A. Squire, D. J. Goodman, A. M. Cowan, and S. C. Moore (1988). The attenuation rates of ocean waves in the marginal ice zone, *J. of Geophys. Res.*, **93**, 6799–6818.
Wadhams, P. and J. Thomson (2015). The Arctic Ocean cruise of R/V Sikuliaq 2015, An investigation of waves and the advancing ice edge. *Il Polo,* **LXX-4,** 9-38.
Wadhams, P., V. A. Squire, D. J. Goodman, A. M. Cowan, and S. C. Moore (1988). The attenuation rates of ocean waves in the marginal ice zone, *J. of Geophys. Res.*, **93**, 6799–6818.
Wang, R., H. H. Shen (2010). Gravity waves propagating into an ice-covered ocean: A viscoelastic model, *J. Geophys. Res.,* **115**, doi:10.1029/2009JC005591.
The WAVEWATCH III® Development Group (WW3DG) (2016). User manual and system documentation of WAVEWATCH III® version 5.16. Tech. Note 329, NOAA/NWS/NCEP/MMAB, College Park, MD, USA, 326 pp. + Appendices.
Weber, J.E. (1987). Wave attenuation and wave drift in the marginal ice zone. *J. Phys. Oceanogr*., **17**(12), 2351-2361.